Discover Oncology

RESEARCH Open Access

# Multi-omics integration constructs a senescence-based prognostic model and identifies EIF4EBP1 as a therapeutic target in clear cell renal cell carcinoma

He Duan[1,2†], Ning Li[3†], Dingming Song[1], Yongzhuo Li[4], Xin Liang[2], Yongxue Ding[5*] and Ming Tong[1*]

[†]He Duan and Ning Li contributed equally to this work.

*Correspondence:
Yongxue Ding
dalingyongxue@163.com
Ming Tong
tongming@jzmu.edu.cn
[1]Department of Urology, The First Affiliated Hospital of Jinzhou Medical University, Jinzhou, China
[2]Department of Urology, General Hospital of Fushun Mining Bureau of Liaoning Health Industry Group, Fushun, China
[3]Cancer Center and Center of Translational Medicine, The First Affiliated Hospital of Jinzhou Medical University, Jinzhou, China
[4]Department of Gastroenterology, The First Affiliated Hospital of Jinzhou Medical University, Jinzhou, China
[5]Department of Urology, Liaoyang City Central Hospital, Liaoyang, China

## Abstract

**Introduction** Clear cell renal cell carcinoma (ccRCC) is a prevalent malignancy of the kidney, known for its aggressive growth and tendency to metastasize. Cellular senescence (CS), regarded as a characteristic feature of the natural aging process, is strongly linked to the initiation and advancement of several diseases. This research seeks to develop an integrated prognostic model utilizing senescence markers in ccRCC, with the goal of evaluating clinical outcomes and clarifying the tumor's immune microenvironment.

**Methods** The transcriptome profiles from ccRCC patients were acquired from TCGA database, and the senescence-related genetic model (SRGM) was developed through Cox proportional hazards analysis integrated with multiple machine learning approaches. In addition, immune microenvironment and drug sensitivity analysis were performed. EIF4EBP1 expression and its role in epithelial cell senescence were analyzed using single-cell RNA sequencing, spatial transcriptomics, and trajectory analysis. Finally, cellular experiments were conducted to confirm the role of silencing EIF4EBP1 in the biological behavior of ccRCC cells.

**Results** Through a comprehensive framework incorporating 117 machine learning algorithm combinations, we established an SRGM consisting of 9 genes. The optimal model was constructed using CoxBoost + StepCox[forward] and achieved a concordance index (C-index) of 0.743, demonstrating robust prognostic predictive capacity across independent datasets. EIF4EBP1 is a central gene in the model. Silencing EIF4EBP1 reduced cell migration, proliferation, and invasion, while inducing senescence-associated phenotypes and apoptosis in ccRCC cells. Additionally, it significantly enhanced the responsiveness of ccRCC cells to sunitinib treatment.

**Conclusions** In summary, we developed a novel SRGM that effectively stratifies prognosis in ccRCC. Furthermore, EIF4EBP1 has been validated at the cellular level as a promising therapeutic target, providing innovative insights into the personalized treatment of ccRCC.

**Keywords** Machine learning, Cellular senescence, Clear cell renal cell carcinoma, Spatial transcriptomics, EIF4EBP1, Single-cell, Prognostic model

## 1 Background

ccRCC is the most common subtype of renal cell carcinoma (RCC), comprising approximately 70–90% of renal malignancies [1–3]. Patients diagnosed with early-stage ccRCC typically have favorable outcomes after surgical resection. In contrast, individuals with advanced-stage ccRCC frequently experience recurrence and metastasis, requiring targeted therapy or immunotherapy. However, many of these patients develop resistance to these treatments, leading to an unfavorable prognosis [4, 5]. Recent years have seen substantial advancements in immune checkpoint inhibitors (ICIs) and immunotherapy for ccRCC treatment, leading to notable improvements in the prognosis of certain patients. However, the heterogeneity of the tumor microenvironment (TME) leads to differential responses to immune checkpoint inhibitor (ICI) treatment, with many patients eventually developing resistance [6, 7]. Accumulating evidence indicates that tumor microenvironment–associated cell programs, including cellular senescence and mesenchymal stem cell–related phenotypes, contribute to ccRCC progression and therapeutic resistance. Importantly, these programs are closely intertwined with metabolic reprogramming in ccRCC, particularly altered energy metabolism and mitochondrial dysfunction, which shape tumor evolution and treatment response [8, 9].Mesenchymal stem cell–related gene signatures have been identified as independent prognostic markers and linked to fibroblast abundance and immunotherapy response [10]. Together with evidence supporting the prognostic relevance of senescence-related mechanisms in ccRCC [11], these findings provide a biological rationale for developing senescence-related gene models in ccRCC. Therefore, the development of reliable molecular biomarkers and prognostic models to support early diagnosis and personalized treatment decisions has become a key challenge.

CS refers to a stable, stress-triggered state characterized by irreversible cell cycle arrest and accompanied by heightened secretion of factors constituting the senescence-associated secretory phenotype (SASP). This phenomenon significantly alters the TME, influencing tumor growth, angiogenesis, and immune evasion [12]. CS is regarded as a double-edged sword, as it has been shown to exert both tumor-suppressive and oncogenic effects, depending on the surrounding environment [13–15]. In the early stages of cancer, CS may play a protective role by suppressing tumorigenesis. However, during tumor progression, particularly in cells with a prominent SASP, CS promotes cancer cell invasion and distant metastasis [16, 17]. As aging progresses, CS accumulates and correlates exponentially with the incidence and mortality of various cancer types [18]. CS contributes to the pathogenesis of various degenerative disorders, primarily through mechanisms involving cellular and tissue dysfunction. These pathological effects include dysregulated cell proliferation, apoptotic induction, reactive oxygen species accumulation, and oxidative stress, ultimately resulting in DNA damage [19–21].

In this study, we developed a novel SRGM using bioinformatics tools to clarify the role of CS in ccRCC progression and guide individualized treatment optimization. The research flow chart is shown in Fig. 1.

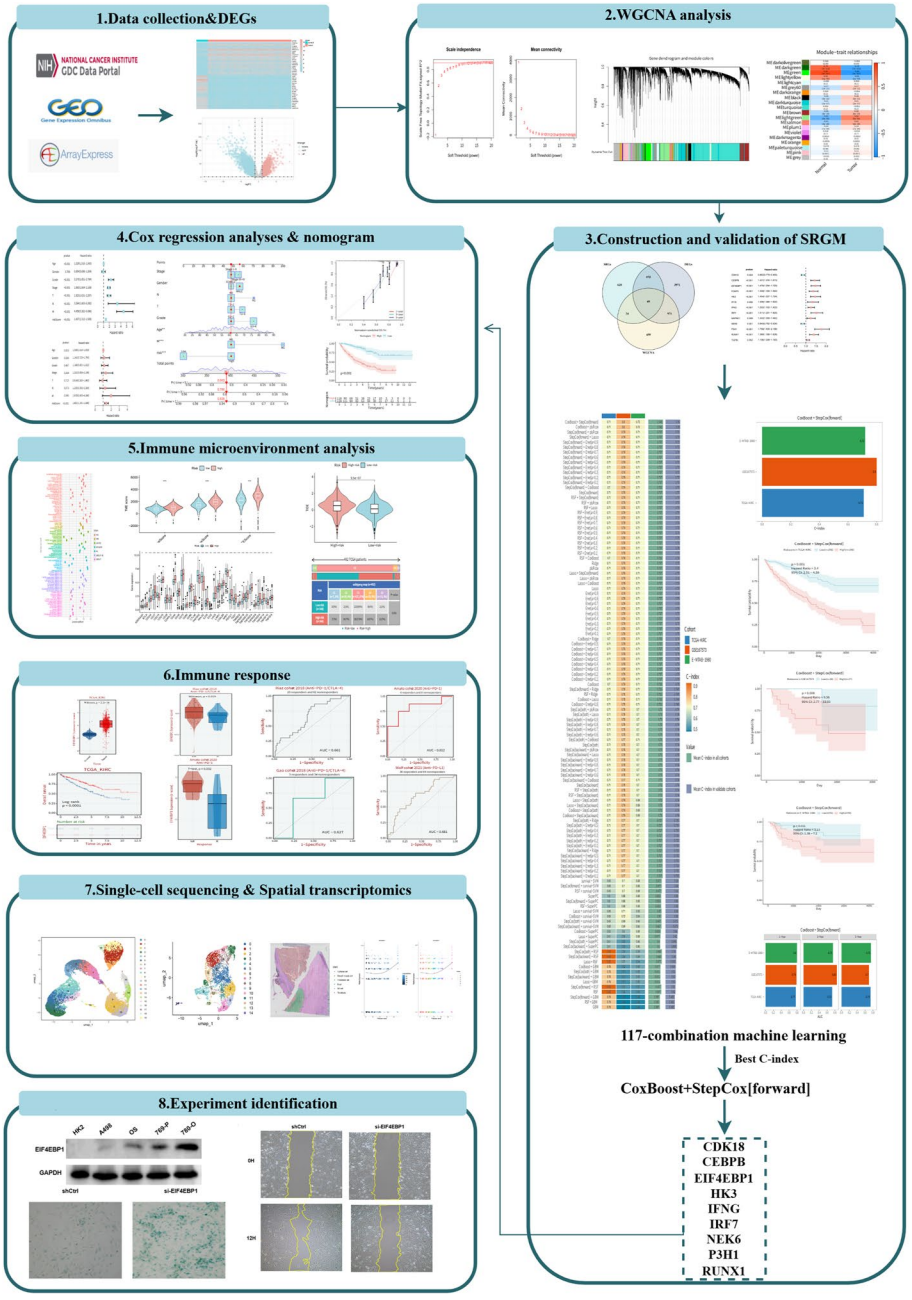


**Fig. 1** A flow chart of the study

## 2 Materials and methods

### 2.1 Data acquisition

The training dataset for ccRCC was sourced from the TCGA-KIRC cohort. RNA expression profiles, along with associated clinical data for ccRCC, were retrieved from the TCGA database (https://portal.gdc.cancer.gov/), comprising 541 tumor samples and 72 normal tissue specimens. The validation set for ccRCC was derived from the GEO database (https://www.ncbi.nlm.nih.gov/geo/) and the ArrayExpress repository (https://www.ebi.ac.uk/arrayexpress/), with the GSE167573 cohort encompassing 55 ccRCC samples and the E-MTAB-1980 cohort containing 101 ccRCC samples. Senescence-associated genes (SRGs) were obtained from the CellAge database (https://genomics.senescence.i

nfo/cells/, accessed on October 18, 2024). The gene list was downloaded and locked at the time of access and used consistently for all subsequent analyses, without incorporating any later database updates, to ensure data consistency and reproducibility. Single-cell RNA sequencing (scRNA-seq) data were acquired from the GSE224630 dataset, which includes six ccRCC samples. Additionally, the spatial transcriptomics (ST) data, GSE210041, were retrieved from the GEO database.

### 2.2 Differentially expressed genes and WGCNA

Differentially expressed genes (DEGs) between ccRCC tumor samples and matched normal tissues were identified using the "limma" R package. DEGs were defined as those with $P < 0.05$ and $|\log_2 FC| > 1$. Next, gene co-expression networks for the TCGA-KIRC dataset were built using the "WGCNA" R package, a method for dimensionality reduction and unsupervised classification. We chose a soft threshold power of 11 for gene network construction, calculating co-expression similarity and gene adjacency before conversion to a Topological Overlap Matrix (TOM). Gene modules were clustered using TOM-based hierarchical analysis. Module-clinical trait correlations were then visualized through heatmap analysis.

### 2.3 Core gene screening and enrichment analysis

Venn diagrams were generated using the "VennDiagram" package to identify genes shared between SRGs, DEGs, and genes from the WGCNA lightgreen module. Functional enrichment analyses of Gene Ontology (GO) terms and Kyoto Encyclopedia of Genes and Genomes (KEGG) pathways were conducted using the R packages "clusterProfiler", with visualizations generated by "ggplot2".

### 2.4 Prognostic model development

The prognostic model was constructed using the "Mime1" package [22], which includes ten classic machine learning algorithms: Enet, RSF, StepCox, superpc, plsRcox, CoxBoost, GBM, survivalsvm, Lasso, and Ridge. The model construction proceeded as follows: univariate Cox regression analysis was conducted to screen senescence-related genes meeting the threshold of $p < 0.01$. Next, 117 algorithms were generated by combining 10 machine learning techniques, aiming to develop the most effective predictive system with superior c-index performance.

### 2.5 Evaluation of the prognostic model

Fifty-five published ccRCC signatures (see Tables S1–S2) were evaluated across the training and external validation cohorts to calculate the concordance index (C-index). Patients across the training and testing sets were categorized into high- or low-risk subgroups using median risk scores, and Kaplan-Meier curves were generated to assess survival differences in each cohort. Univariate Cox regression was applied to the final model, followed by a meta-analysis combining the training and validation datasets. Time-dependent ROC analysis evaluated the risk model's predictive performance and association with clinicopathological variables at 1-, 3-, and 5-year intervals. The "rms" R package was used to develop nomograms, and calibration curves were employed to evaluate their performance.

### 2.6 Immune landscape analysis

Correlations of risk scores with tumor-infiltrating immune cells (TIICs) were examined through seven algorithms: TIMER, XCELL, QUANTISEQ, EPIC, MCPCOUNTER, CIBERSORT-ABS, and CIBERSORT. Immune cell proportions in tumor samples were determined with the CIBERSORT algorithm, quantifying 22 immune cell types. The TIDE algorithm (http://tide.dfci.harvard.edu/) predicted ICI response by integrating T-cell dysfunction, exclusion, and myeloid suppression signatures, where lower scores indicate better treatment response. Stromal, immune, and estimate scores were computed using the "ESTIMATE" R package to quantify the TME composition across TCGA-KIRC samples. In addition, immune subtypes (C1–C6) were defined according to the pan-cancer immune classification framework originally described by Thorsson and colleagues, and immune subtype labels for TCGA-KIRC samples were obtained from publicly available TCGA immune subtype annotations derived from gene expression–based immune signatures [23].

### 2.7 Drug sensitivity analysis

The half-maximal inhibitory concentration (IC50) values were analyzed with the "oncoPredict" package. Drugs showing statistically significant differences in their effects between high- and low-risk patient groups were chosen for further evaluation.

### 2.8 Survival analysis

To validate the association between prognostic gene signatures and survival outcomes, the BEST platform (https://rookieutopia.com/app_direct/BEST) was employed. Furthe rmore, leveraging multiple independent cohorts (Gao, Wolf, Amato, and Riaz) from the BEST database, a comprehensive drug-target interaction analysis was conducted.

### 2.9 Single-cell RNA sequencing analysis

The Seurat R package was employed to process scRNA-seq data. The LogNormalize method was applied for data normalization, followed by the identification of 2000 highly variable genes. After reducing dimensionality with principal component analysis (PCA), both t-distributed stochastic neighbor embedding (t-SNE) and uniform manifold approximation and projection (UMAP) were applied for dimensionality reduction, with UMAP used for visualization in the final figures. To correct for batch effects across samples, the Harmony algorithm was applied. Cell clustering was performed using the "FindClusters" function with multiple resolution parameters, and the optimal clustering result was selected accordingly. Differentially expressed marker genes for each cluster were identified using the "FindAllMarkers" function. Cell type annotation was conducted using the "SingleR" package in combination with manual annotation, with detailed results provided in Supplementary Table S3. The expression pattern of EIF4EBP1 across different cell clusters and annotated cell types was visualized using "FeaturePlot" and "VlnPlot". Based on detectable EIF4EBP1 expression, cells were categorized into EIF4EBP1-positive and EIF4EBP1-negative groups, and the relative proportions of major cell types were compared between the two groups. Finally, cell trajectory analysis was performed using the "Vector" package to infer potential cellular developmental trajectories [24].

### 2.10 Spatial transcriptomics analysis

ST data were examined using the "Seurat" R package. Data were normalized using the "SCTransform" function, and dimensionality reduction was performed using the "RunPCA" method. The "SpatialDimPlot" function was employed for visualizing cell clustering and dimensionality reduction analysis. The "spacexr" R package, which performs RCTD deconvolution analysis, was used to integrate ST data with scRNA-seq data. Additionally, the "scMetabolism" R package was used for metabolic profiling analysis of ST data [25]. "Monocle (v2)" was employed to investigate pseudotime trajectories of epithelial cell populations in the spatial transcriptomics dataset. The "reduceDimension (DDRTree)", "orderCells", and "plot_cell_trajectory" functions were used to compute and visualize these pseudotime trajectories.

### 2.11 Cell culture and transfection

The ccRCC cell lines (OS-RC-2, 786-O, 769-P, and A498) and the human renal tubular epithelial cell line (HK-2) were purchased from the Chinese Academy of Sciences (Shanghai, China). Cells were cultured in RPMI-1640 medium with 10% FBS (Gibco, USA) at 37 °C in a 5% $CO_2$ incubator. Small interfering RNA (siRNA) targeting human EIF4EBP1 (si-EIF4EBP1) and a non-targeting control siRNA (si-Ctrl) were obtained from GenePharma (Shanghai, China). The si-Ctrl does not target any known human gene and was used to control for potential off-target effects of siRNA transfection. 786-O cells were transfected with siRNA using the siRNA-Mate™ transfection reagent (GenePharma, Shanghai, China). After 48 h, transfection efficiency was evaluated by Western blotting. Supplementary Table S4 lists the siRNA sequences used.

### 2.12 qRT-PCR detection

Total RNA was extracted using the RNAeasy RNA Kit (Beyotime, Shanghai, China), and cDNA was synthesized with NovoScript® Plus one-step 1st Strand cDNA Synthesis SuperMix (Cat#E147-01 A, Novoprotein, Shanghai, China). qRT-PCR was conducted using SYBR High-Sensitivity qPCR SuperMix (Cat#E099, Novoprotein, Shanghai, China) in triplicate, and relativeElF4EBP1 expression levels were calculated using the 2-ΔΔCT method. Primer sequences are provided in Supplementary Table S5.

### 2.13 Western blotting

Total cellular proteins were extracted with RIPA lysis buffer (Beyotime, Shanghai, China), supplemented with PMSF (Beyotime, Shanghai, China) to further inhibit protease activity. Protein lysates were electrophoresed through 10% SDS-PAGE and transferred to PVDF membranes. Membranes were blocked with skim milk for 1 h at room temperature, incubated with primary antibodies overnight at 4 °C, then with secondary antibodies for 2 h after washing. Signal detection was carried out using an enhanced chemiluminescence reagent (Sevenbio, Beijing, China), and band quantification was conducted with ImageJ software. Supplementary Table S6 contains all antibody information.

### 2.14 Transwell migration and invasion assays

Transwell migration and invasion assays were performed using 24-well Transwell chambers (Corning, USA). 786-O cells ($2 \times 10^4$) suspended in 150 µL serum-free medium were seeded into the upper chambers, which were pre-coated with Matrigel (Corning, USA)

for invasion assays. The lower chambers contained 600 μL medium supplemented with 10% FBS. Cells were incubated at 37 °C with 5% $CO_2$ for 24 h. Cells on the lower surface were then fixed and stained, and migrated or invaded cells were imaged and quantified using ImageJ software.

### 2.15 Wound healing assay

The 786-O cells, transfected as described, were plated in 6-well plates and cultured until they reached 90% confluence. A sterile 200 μL pipette tip was used to create a scratch, and microscopic images were captured at 0 and 12-h intervals. Wound healing was analyzed with ImageJ software.

### 2.16 Cell proliferation assay

EIF4EBP1-knockdown 786-O cells and their parental cells were seeded in 96-well plates at a density of $3 \times 10^3$ cells per well. After allowing the cells to adhere, they were cultured for 0, 12, or 24 h. At each time point, 10 μL of CCK-8 reagent (NCM Biotech, Suzhou, China) was added to each well, followed by incubation at 37 °C for 2 h. Absorbance was then measured at a wavelength of 450 nm.

### 2.17 Apoptosis assay

Cellular apoptosis was evaluated using PE-conjugated Annexin V (BD Pharmingen, USA) and 7-aminoactinomycin D (7-AAD). Briefly, a cell suspension of $1 \times 10^5$ cells was collected, rinsed with PBS, and then resuspended. The cells were treated with 5 μL of PE-conjugated Annexin V and 7-AAD for 15–20 min in the dark at room temperature, and apoptosis was assessed using flow cytometry (Becton Dickinson, USA).

### 2.18 SA-β-Gal staining

SA-β-Gal staining was performed following the manufacturer's instructions (Beyotime, Shanghai, China). Briefly, cells were collected, rinsed with PBS, fixed with 1 mL of β-galactosidase staining solution for 15 min, and then rinsed three times with PBS. The cells were incubated overnight at 37 °C with 1 mL of working staining solution. Images were captured by microscopy, and analysis was performed using ImageJ software.

### 2.19 Sunitinib drug test

Sunitinib was obtained from Aladdin (Shanghai, China). Cells were seeded in 6-well plates and treated with varying doses of sunitinib after 12 h. After 48 h, optical density (OD) was measured using a spectrophotometer. For colony formation assays, cells were resuspended in RPMI-1640 and plated at $5 \times 10^3$ cells per well. After 2 weeks of culture, cells were fixed with 4% paraformaldehyde for 20 min and stained with 0.1% crystal violet (Beyotime, Shanghai, China) for 15 min. Colonies were first photographed and then quantified separately using ImageJ software.

### 2.20 Tissue specimens and immunohistochemistry

Clinical samples were collected from the First Affiliated Hospital of Jinzhou Medical University between March and October 2024, including 15 pairs of ccRCC and adjacent non-cancerous tissues. Informed consent was obtained from all patients, and the study was approved by the hospital's Ethics Committee (Reference No.KYLL202513).

Tissue sections were deparaffinized with xylene, rehydrated with ethanol, and subjected to antigen retrieval in citrate buffer. Sections were incubated with 25 μL of goat serum (G1208-5ML, Servicebio, China) for 1 hour, followed by overnight incubation with anti-EIF4EBP1 antibody at 4°C. Following PBS washing, sections were incubated with HRP-conjugated secondary antibody for 30 minutes, stained with 3,3'-diaminobenzidine (DAB) reagent (ZSGB-BIO, China), counterstained with hematoxylin, and imaged under a microscope.

### 2.21 Pan-cancer analysis of EIF4EBP1 expression and its prognostic significance

RNA sequencing (RNA-seq) data of EIF4EBP1 and corresponding clinical information for 33 cancer types were obtained from The Cancer Genome Atlas (TCGA). Tumor and available normal samples were included. Samples with EIF4EBP1 expression values equal to zero were excluded, and expression data were log2-transformed. EIF4EBP1 expression patterns across tumor and normal tissues were visualized using the "ggplot2" R package. Prognostic value was evaluated using TCGA survival data by stratifying patients into high- and low-expression groups based on the median EIF4EBP1 expression level. Cox proportional hazards regression and Kaplan–Meier survival analyses were performed to assess overall survival, with hazard ratios (HRs), 95% confidence intervals (CIs), and log-rank p values calculated. Forest plots were used to summarize survival risks across cancer types.

### 2.22 Data processing

Statistical analyses were conducted using GraphPad Prism (version 10.1.2) and R software (version 4.2.2). All in vitro experiments were performed in at least three independent biological replicates. Quantitative data are presented as the mean ± standard deviation (SD). Group differences were evaluated using paired or unpaired Student's *t*-tests, Wilcoxon tests, or one-way analysis of variance (ANOVA), as appropriate. Spearman correlation analysis was applied to assess correlations. A $P$ value $< 0.05$ was considered statistically significant.

## 3 Results

### 3.1 Differentially expressed genes related to cellular senescence in clear cell renal cell carcinoma

We performed a differential expression analysis of tumor and normal tissues using the TCGA-KIRC dataset, identifying 2184 upregulated and 2980 downregulated genes (Fig. 2A and B). We then performed WGCNA using a soft-thresholding power β of 11, which resulted in a scale-free topology suitable for further analysis (Fig. S1A and B). The results revealed that the lightgreen module showed the most significant positive correlation with the tumor (Fig. 2C). By intersecting DEGs, SRGs, and the lightgreen module, we identified 49 overlapping genes (Fig. 2D).

### 3.2 Enrichment analysis of overlapping genes

We conducted GO and KEGG enrichment analyses to investigate the biological functions linked to the overlapping genes in ccRCC. GO enrichment analysis highlighted key enrichments in biological processes, with monocyte differentiation and cytokine regulation being prominent. In cellular components, extracellular matrix was most significant,

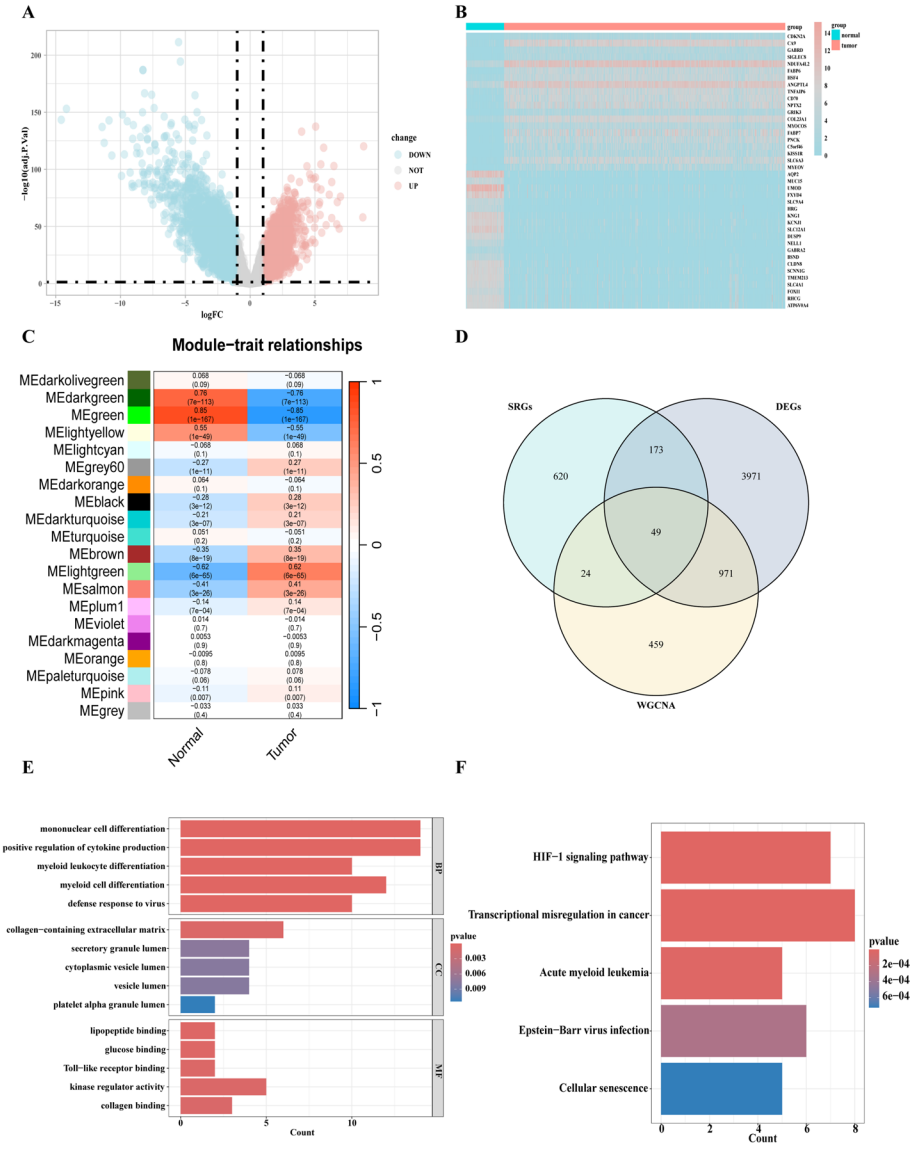


**Fig. 2** Differentially Expressed Genes and WGCNA Analysis. **A** Volcano plot and **B** heatmap of DEGs between ccRCC and normal tissues in the TCGA-KIRC dataset. **C** WGCNA of TCGA-KIRC showing the strongly positively correlated module. **D** Venn diagram displaying the 49 overlapping genes. **E, F** Enrichment analyses of GO terms and KEGG pathways for the 49 overlapping genes.

and in molecular functions, kinase regulation and collagen binding were enriched (Fig. 2E). Additionally, KEGG pathway analysis indicated significant enrichment of the overlapping genes in key pathways such as the HIF-1 signaling pathway, transcriptional dysregulation in cancer, acute myeloid leukemia, Epstein-Barr virus infection, and cellular senescence (Fig. 2F).

### 3.3 Construction of prognostic model based on 9 key genes

Univariate Cox regression identified 13 candidate genes from overlapping genes for prognostic model development (Fig. S1C). We assessed 117 combinations of 10 machine learning algorithms, using TCGA-KIRC for training and validating the model with GSE167573 and E-MTAB-1980 under cross-validation. The combination of CoxBoost + StepCox[forward] performed the best, achieving a peak C-index of 0.743, which

indicates superior predictive accuracy. Reproducible findings in independent cohorts further reinforced its robustness (Fig. 3A). This model contains 9 key genes: CDK18, CEBPB, EIF4EBP1, HK3, IFNG, IRF7, NEK6, P3H1, and RUNX1. Supplementary Table S7 provides a detailed list of the corresponding weights for each gene in the model. While multiple ccRCC prognostic signatures have been developed recently, their predictive performance remains suboptimal. Our risk model demonstrated superior sensitivity and specificity across all three validation cohorts compared to 55 published ccRCC models (Fig. 3B). Time-dependent ROC curves revealed high predictive accuracy (AUC > 0.7) for 1-, 3-, and 5-year survival across all datasets (Fig. 3C). Stratification by median risk score categorized ccRCC cases into high- and low-risk subgroups, with significantly poorer outcomes in the former (Fig. 3D). Meta-analysis of three cohorts (TCGA-KIRC, GSE167573, E-MTAB-1980) revealed a significant prognostic association, with a pooled hazard ratio (HR) of 3.47 (95% CI: 2.53–4.76, $P < 0.001$), suggesting a robust link between the biomarker and patient survival across these cohorts (Fig. 3E). For external validation, we compared our model 55 existing prognostic signatures using identical methodology. The results demonstrated that the constructed model significantly outperformed the other models in terms of prognostic risk discrimination. (Fig. 3F).

### 3.4 Construction and evaluation of the prognostic nomogram

Next, we conducted univariate and multivariate Cox regression analyses to assess the prognostic significance of risk scores and clinical indicators. Figure 4A and B show that both age and risk score are important prognostic factors for ccRCC outcomes in the multivariate analysis. A nomogram was developed by integrating the risk score with clinically relevant features to improve the prediction of overall survival (OS) in these patients (Fig. 4C). The calibration curve revealed strong agreement between the nomogram's predicted 1-, 3-, and 5-year survival rates and the observed outcomes in the TCGA-KIRC cohort (Fig. 4D). ROC curve analysis was used to assess the prognostic performance of multiple clinical variables and the risk score. As shown in Fig. 4E, the AUC of the risk score was 0.770, indicating its ability to distinguish between patients with different prognostic outcomes. Additionally, stratification based on the nomogram's total score categorized ccRCC cases into high- and low-risk groups, with significantly poorer OS in the former (Fig. 4F). The findings suggest that the nomogram is an effective prognostic instrument for ccRCC, allowing clinicians to customize treatment approaches with increased accuracy.

### 3.5 GSEA reveals distinct biological pathways associated with SRGM risk stratification

To investigate the biological functions underlying the SRGM risk stratification in ccRCC, gene set enrichment analysis (GSEA) was performed to compare the high- and low-risk groups defined by the SRGM model. As shown in Supplementary Fig. 2A, the high-risk group was predominantly enriched in immune- and inflammation-related pathways, including chemokine signaling, cytokine–cytokine receptor interaction, systemic lupus erythematosus, as well as ribosome and type I diabetes mellitus. In contrast, the low-risk group exhibited significant enrichment of metabolic and homeostasis-related pathways, such as fatty acid metabolism, peroxisome, PPAR signaling, the renin–angiotensin system, and branched-chain amino acid degradation (Fig.S2B).

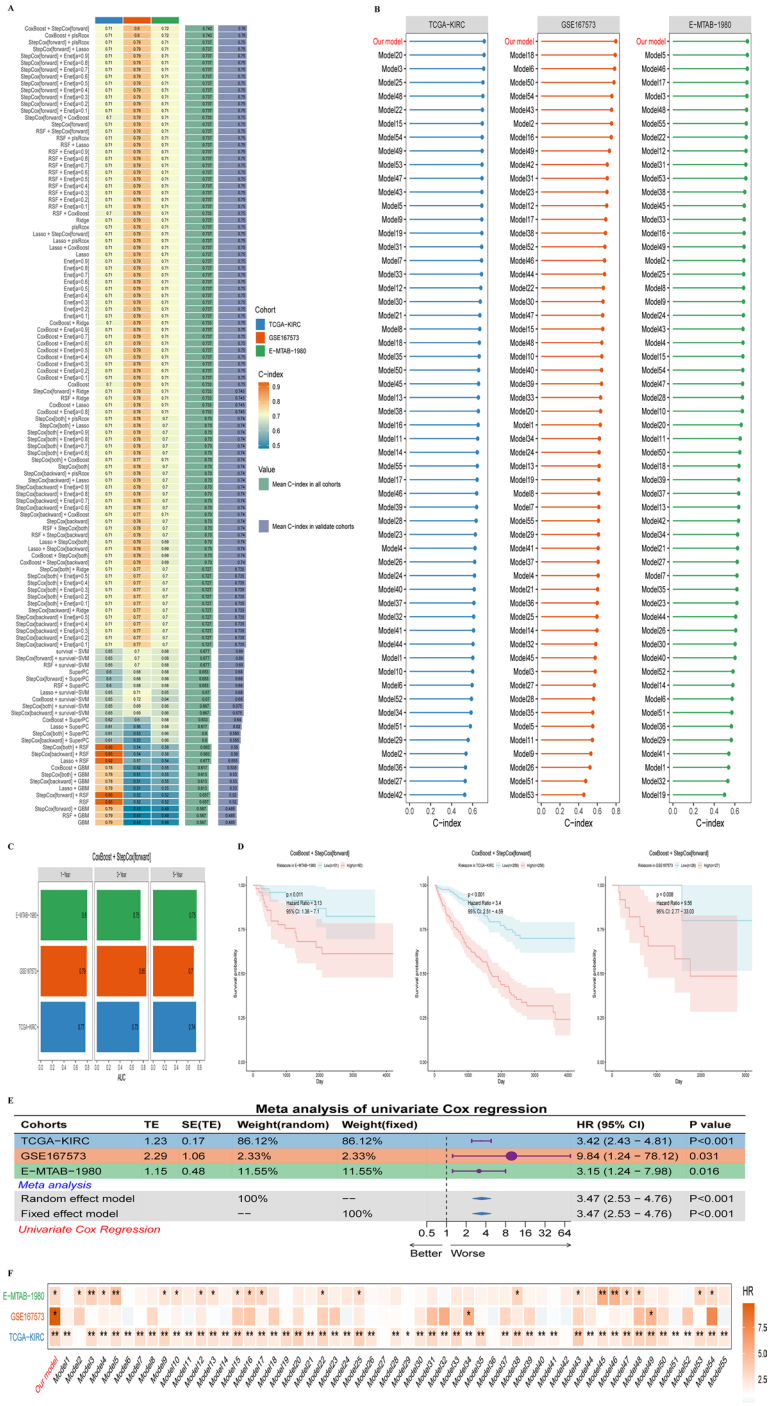


**Fig. 3** Development and Validation of SRGM. **A** C-index across three cohorts derived from the integration of ten machine learning algorithms. **B** Comparison of C-index between TCGA-KIRC, GSE167573, E-MTAB-1980, and 55 previously published ccRCC prognostic models. **C** Time-dependent AUC values at 1, 3, and 5 years for the TCGA-KIRC training cohort and the GSE167573 and E-MTAB-1980 validation cohorts. **D** KM survival curves in different cohorts. **E** Meta-analysis of univariate Cox regression across TCGA-KIRC, GSE167573, and E-MTAB-1980 cohorts.**F** Univariate Cox Regression Meta-Analysis of ccRCC Prognostic Models in Three Cohorts. (*$p < 0.05$, **$p < 0.01$)

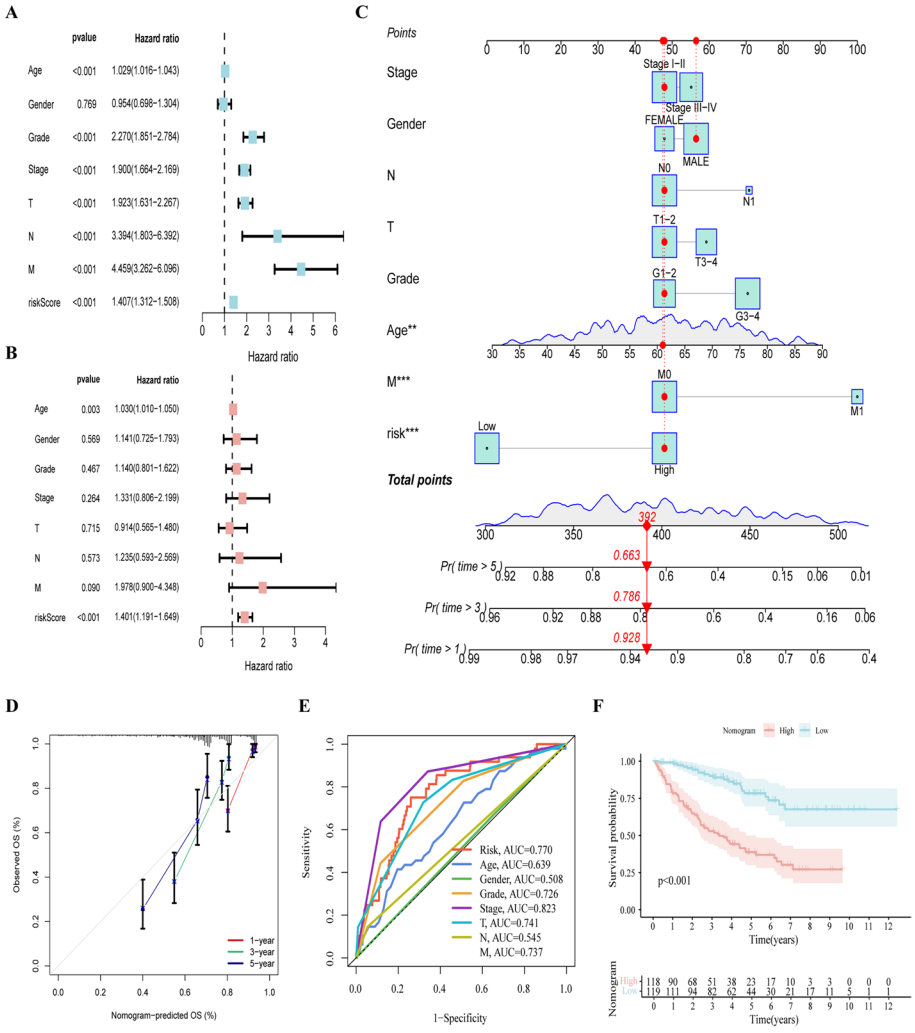


**Fig. 4** Development of a Predictive Nomogram. **A, B** Forest plots showing the association of clinicopathological features and risk score with prognosis, based on univariate and multivariate Cox regression analyses. **C** A nomogram developed to predict the overall survival of ccRCC patients in the TCGA-KIRC cohort. **D** Calibration curve for nomogram-predicted 1-, 3-, and 5-year overall survival in ccRCC patients. **E** ROC curves comparing the predictive performance of risk score and clinical features. **F** KM survival curve for OS prediction based on the nomogram

### 3.6 The prognostic model exhibits a high-risk tendency for multiple immune checkpoints

TME interactions with cancer cells are crucial during cancer formation and progression [26]. Notably, TIICs contribute substantially to this process [27, 28]. To evaluate the association between the SRGM risk score and TIICs, we used seven immune infiltration algorithms and compared immune cell distribution patterns across methodologies (Fig. 5A). Analysis demonstrated significant positive correlations between higher risk scores and increased infiltration of most immune cell types in tumor tissues. CIBERSORT analysis revealed distinct immune infiltration profiles between the risk groups. High-risk patients showed elevated Tregs, plasma cells, and M0 macrophages, while low-risk patients exhibited higher levels of CD4 memory resting T cells, resting mast cells, and resting dendritic cells (Fig. 5B). Next, we Used the ESTIMATE algorithm to assess the immune score, stromal score, and estimate score for both groups. The results revealed that the low-risk group had notably lower scores in all three metrics compared to the high-risk group (Fig. 5C). We further examined the distribution of SRGM risk groups

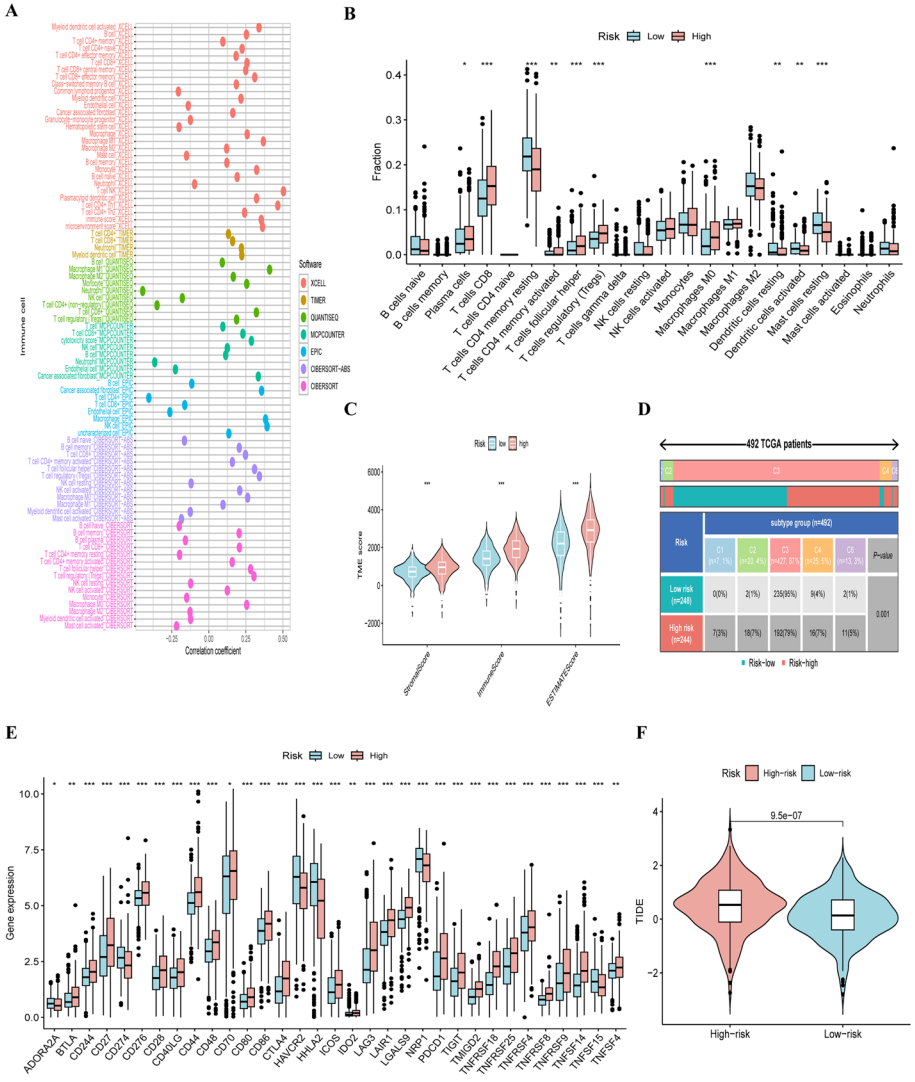


**Fig. 5** Immunological Feature Analysis of the Prognostic Model. **A** The association between risk score and immune cell infiltration. **B** CIBERSORT boxplot comparison between high-risk and low-risk groups. **C** Analysis of the TME. **D** Distribution of SRGM risk groups (high-risk and low-risk) across TCGA immune subtypes (C1–C6). C1, Wound Healing; C2, IFN-γ Dominant; C3, Inflammatory; C4, Lymphocyte Depleted; C5, Immunologically Quiet; C6, TGF-β Dominant. C5 was not observed in the TCGA-KIRC cohort. **E** Expression levels of immune checkpoints in high-risk and low-risk patients. **F** TIDE analysis comparing high-risk and low-risk groups. (*$p < 0.05$, **$p < 0.01$, ***$p < 0.001$)

across TCGA immune subtypes. Immune subtypes were defined according to the pan-cancer immune classification, including C1 (Wound Healing), C2 (IFN-γ Dominant), C3 (Inflammatory), C4 (Lymphocyte Depleted), C5 (Immunologically Quiet), and C6 (TGF-β Dominant). As shown in Fig. 5D, the distribution of SRGM risk groups (high-risk and low-risk) differed significantly across immune subtypes ($P$ = 0.001), highlighting the close association between SRGM stratification and the immune microenvironment.

### 3.7 Immune checkpoint expression and prediction of immunotherapy efficacy

The field of oncology has witnessed transformative progress through ICIs, which effectively strengthen the body's antitumor defenses and enhance clinical outcomes [29]. Immunotherapy biomarker profiling demonstrated that high-risk SRGM patients had significantly elevated expression levels of critical immune checkpoint proteins, including

CTLA-4, TIGIT, PDCD1, and LAG3 (Fig. 5E). This pattern suggests enhanced immune regulatory activity in these patients. Using the TIDE algorithm, we evaluated immunotherapy response potential and observed substantially higher TIDE scores in the high-risk group compared to the low-risk cohort (Fig. 5F).

### 3.8 Comparison of drug sensitivity in different risk subgroups

We compared anticancer drug responses across risk strata by assessing IC50 values for nine agents, visualized using box plots. Low-risk patients showed heightened sensitivity to afatinib, ibrutinib, and osimertinib, while high-risk patients responded better to dasatinib, dabrafenib, fludarabine, fulvestrant, gemcitabine, and 5-fluorouracil (Fig.S3A-I). The SRGM scoring system not only predicts patient prognosis but also shows significant potential for guiding personalized treatment regimens.

### 3.9 EIF4EBP1 exhibits key high-risk tendency in the model

Given that EIF4EBP1 carries the highest weight in the SRGM model, we conducted an in-depth analysis to explore its role further. BEST database analysis showed markedly higher EIF4EBP1 levels in tumors versus normal tissues (Fig. 6A). Patients with elevated EIF4EBP1 exhibited significantly worse survival, indicating its prognostic relevance in ccRCC (Fig. 6B). High EIF4EBP1 expression also correlated with advanced disease features, including higher TNM stage, clinical progression, and poorer histological differentiation (Fig. 6C -G). In addition, correlation analysis revealed that EIF4EBP1 expression was significantly associated with other genes included in the SRGM model, suggesting its potential involvement in coordinated regulatory networks (Supplementary Fig.S4 ).

### 3.10 Elevated EIF4EBP1 expression correlates with poor immunotherapy efficacy

We used the BEST online platform to assess the differential expression of EIF4EBP1 across multiple immunotherapy cohorts and its potential as a candidate biomarker. Both the Riaz and Amato cohorts showed differential EIF4EBP1 expression between immunotherapy responders and non-responders, supporting an association with treatment response (Fig. 6H and I). AUC analysis of across Riaz, GAO, Wolf, and Amato cohorts further demonstrated that elevated EIF4EBP1 levels were associated with poorer responses to PD-1/CTLA-4/PD-L1 blockade (Fig. 6J–M).

### 3.11 Single-cell transcriptomics reveal the association of EIF4EBP1 with senescence-associated cellular programs

UMAP analysis of scRNA-seq data revealed 20 distinct clusters (Fig. 7A). Differential expression profiling identified six primary cell types: epithelial, endothelial, NK, fibroblasts, B cells, and smooth muscle cells (Fig. 7B). A focused analysis of EIF4EBP1 expression in these cell types highlighted significant expression in epithelial cells (Fig. 7C). Composition analysis showed a marked enrichment of epithelial cells in EIF4EBP1-high samples, implicating its potential role in tumor proliferation (Fig. 7D). To support the tumor association of these epithelial populations, we examined the expression of canonical ccRCC tumor markers, including CA9, PAX8, ENPP3, and CD70, at the single-cell level. Per-cluster Feature plots demonstrated concordant enrichment of these established ccRCC markers within the same epithelial clusters exhibiting high EIF4EBP1 expression, thereby supporting their tumor-associated epithelial identity (Supplementary Fig.S5). To

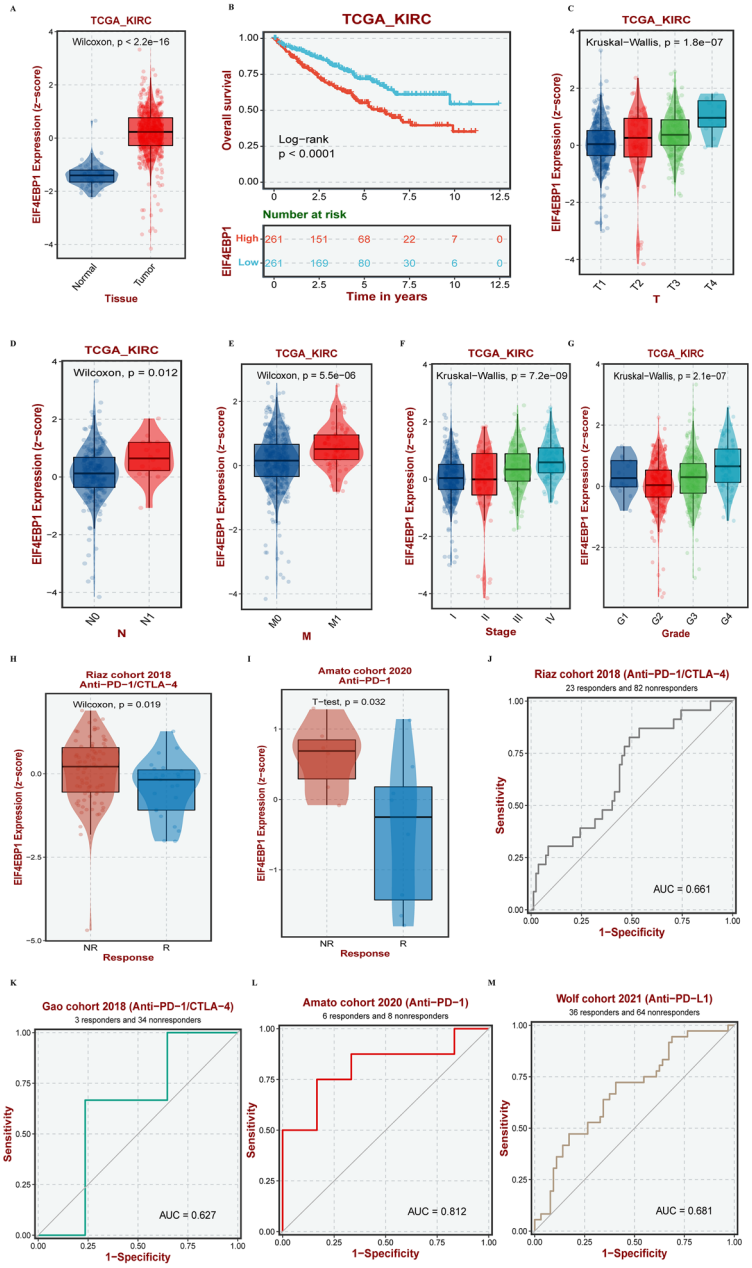


**Fig. 6** EIF4EBP1 expression, survival, and immunotherapy prediction analysis. **A** EIF4EBP1 expression differences between tumor and adjacent normal tissues in TCGA-KIRC.**B** Analysis of OS in relation to EIF4EBP1 expression. **C-G** EIF4EBP1 expression was analyzed in relation to clinicopathological characteristics in the TCGA-KIRC cohort, including T stage, N stage, M stage, pathological stage, and tumor grade.**H, I** Correlation analysis between EIF4EBP1 expression and immunotherapy. **J–M** Immunotherapy sensitivity prediction across different cohorts

explore EIF4EBP1's function in epithelial cells, the epithelial subpopulation was isolated, with its expression visualized via UMAP clustering (Fig. 7E and F). Trajectory analysis using the Vector package revealed that EIF4EBP1-high epithelial regions aligned with the developmental endpoint (Fig. 7G). This suggests that EIF4EBP1 expression increases

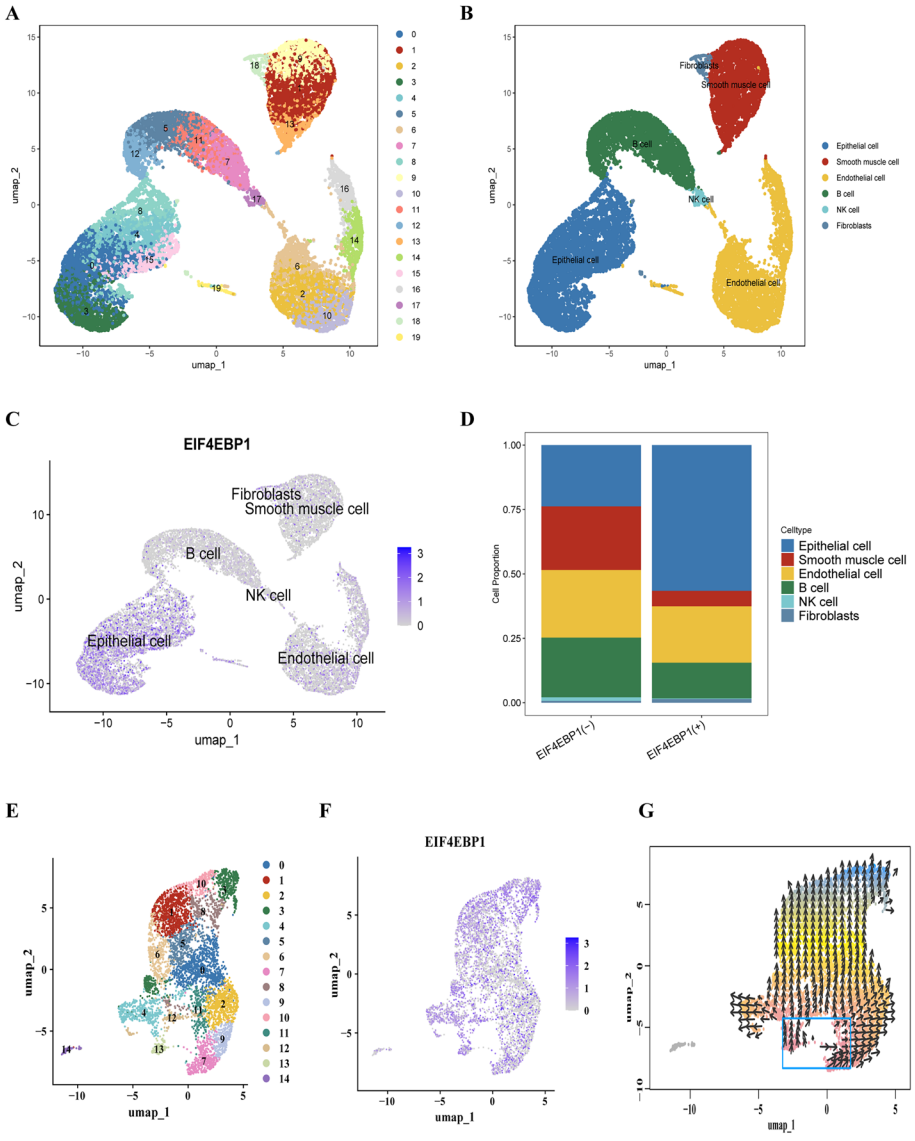


**Fig. 7** Comprehensive single-cell analysis. **A** UMAP plot showing clustering of cells into different groups. **B** UMAP plot identifying cell types in ccRCC. **C** Feature plot visualizing the expression and distribution of EIF4EBP1 in cell clusters. **D** Proportion of cells in different EIF4EBP1 score groups. **E** UMAP plot showing reclustering of epithelial cells into 15 separate clusters. **F** UMAP visualization showing the expression pattern of *EIF4EBP1* across epithelial cell clusters, with color intensity indicating expression levels. **G** Pseudotime analysis depicts the dynamic trajectory of epithelial cells during ccRCC progression

during cellular maturation, a process frequently accompanied by senescence-associated transcriptional and functional programs or cellular exhaustion.

### 3.12 Spatial transcriptomics reveal the expression profile of EIF4EBP1 in epithelial cells

We analyzed the spatial transcriptomics dataset of ccRCC using the Seurat package, normalized the data with SCTransform, and identified 14 clusters. These clusters were projected onto spatial tissue slices to visualize their distribution (Fig. 8A and B). We further investigated the metabolic activity of different cell subtypes using the "scMetabolism" R package and observed elevated activity in clusters 1, 2, 3, 10, and 13 (Fig. 8C). To explore metabolic states across tissue slices, we mapped purine and pyrimidine metabolism and

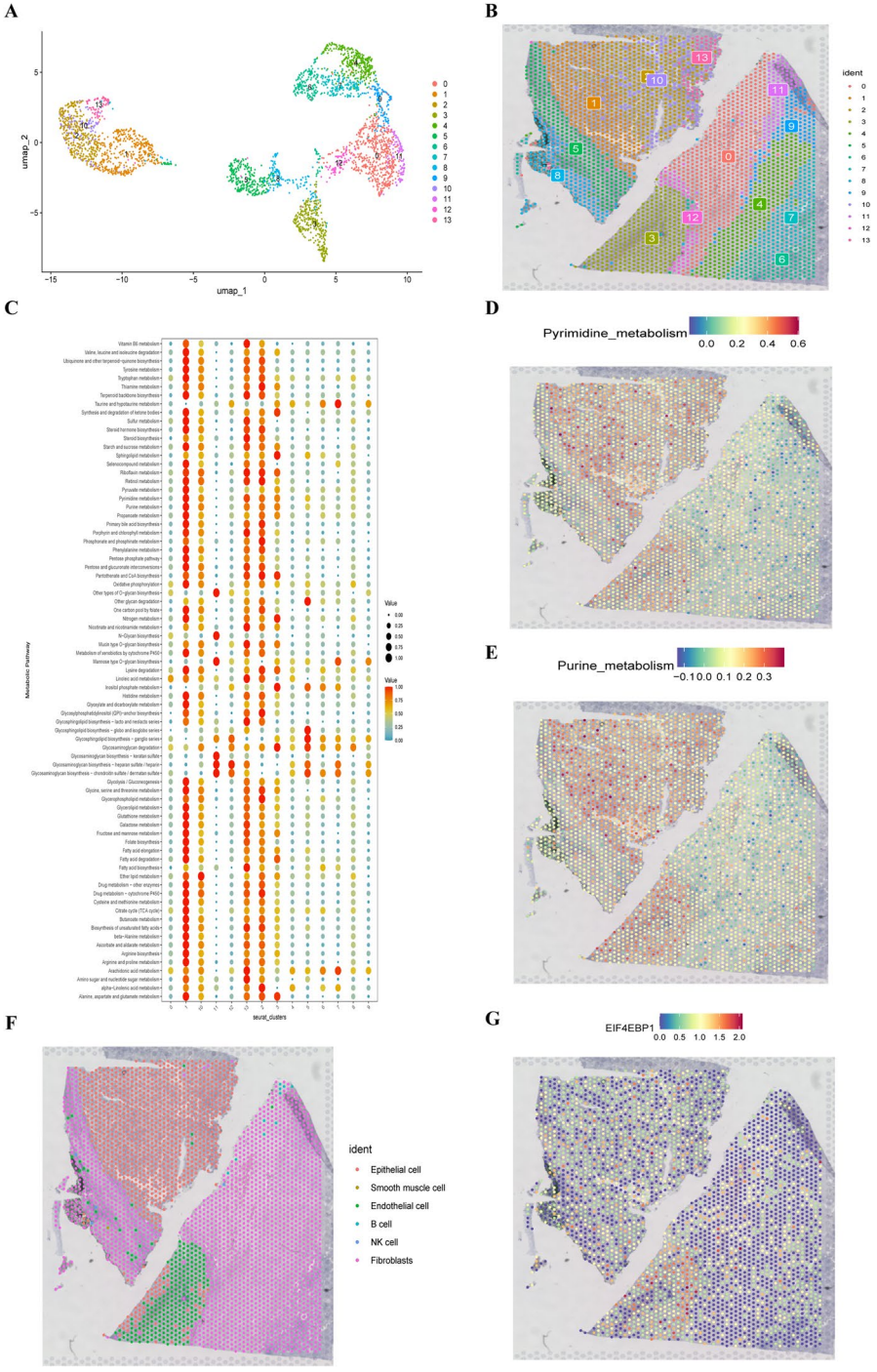


**Fig. 8** ST reveals clusters, metabolism, and EIF4EBP1 expression. **A** UMAP projection and **B** spatial mapping of transcriptional clusters identified by ST. **C** Bubble plot representing metabolic intensity in different clusters. **D** Spatial representation of pyrimidine metabolism intensity. **E** Spatial visualization of purine metabolism intensity. **F** Spatial plot of different cell types obtained through RCTD deconvolution. **G** Spatial distribution of EIF4EBP1 on the spatial transcriptomics tissue section

visualized the varying metabolic activities using heatmaps (Fig. 8D and E). Using RCTD, we mapped cell types annotated by scRNA-seq onto spatial transcriptomics, identifying six distinct spatial clusters (Fig. 8F). A closer examination of EIF4EBP1 expression in spatial transcriptomic slices revealed strong expression in epithelial cells, consistent with our scRNA-seq findings (Fig. 8G).

### 3.13 EIF4EBP1 influences epithelial cell differentiation

Pseudotime trajectory analysis of epithelial cells revealed seven distinct time-state clusters. As pseudotime progressed, the fifth cluster bifurcated into two branches, leading to the sixth and seventh clusters (Fig. 9A-C). Further analysis of EIF4EBP1 expression dynamics during pseudotime revealed peak expression in terminal differentiation stages, implicating its involvement in cellular senescence or late-stage cellular states (Fig. 9D and E).

### 3.14 Pan-cancer expression and prognostic analysis of EIF4EBP1

A pan-cancer analysis leveraging TCGA datasets was performed to systematically assess the expression profiles and prognostic implications of EIF4EBP1 across human malignancies. As shown in Fig.S6A, EIF4EBP1 expression was significantly elevated in tumor tissues relative to corresponding normal controls in the majority of cancer types, including BLCA, BRCA, CESC, CHOL, COAD, ESCA, HNSC, KIRC, KIRP, LIHC, LUAD, LUSC, PRAD, READ, STAD, THCA, and UCEC. Survival analyses demonstrated that increased EIF4EBP1 expression was significantly associated with unfavorable overall survival across multiple cancers (Fig.S6B), with hazard ratios exceeding 1 in most tumor types exhibiting statistically significant associations. Consistent with these findings,

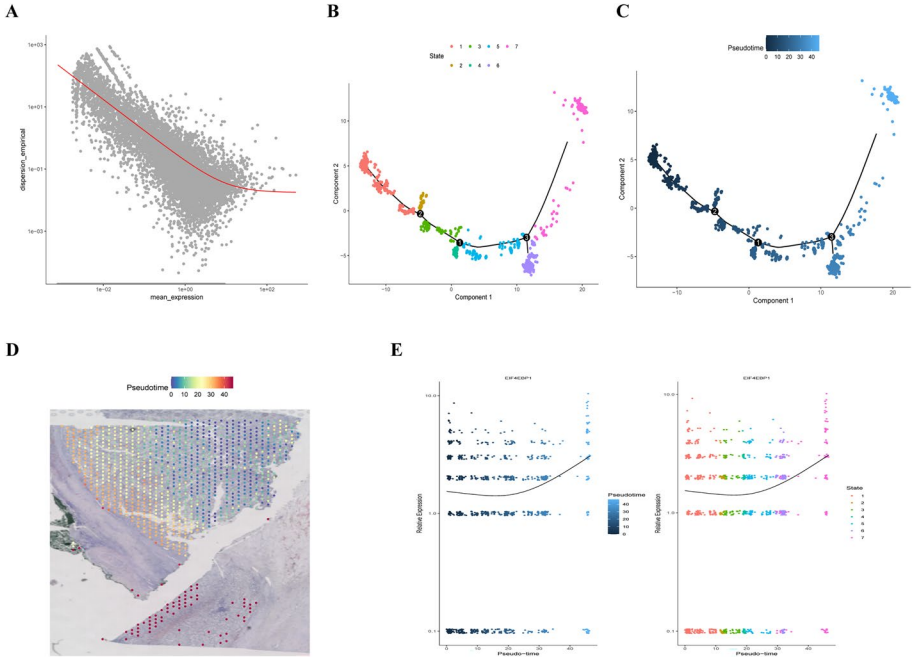


**Fig. 9** Pseudotime and Expression Analysis of Epithelial Cell States. **A** Scatter plot of gene expression (X) versus dispersion (Y) to detect variably expressed genes. **B** Developmental trajectories of the 7 epithelial cell states. **C** Proposed pseudotime progression of the 7 cell clusters, with time progression indicated from black to blue along the trajectory. **D** Spatial distribution of epithelial cells in pseudotime on the tissue section. **E** Expression trend of EIF4EBP1 in the trajectory analysis

Kaplan–Meier analyses (Fig.S6C) revealed that patients with high EIF4EBP1 expression experienced significantly reduced overall survival in BRCA, CESC, GBM, LIHC, LUAD, LUSC, SARC, and UVM. Collectively, these results indicate that EIF4EBP1 is broadly dysregulated across human cancers and may serve as a potential adverse prognostic biomarker in a pan-cancer context.

### 3.15 Knockdown of EIF4EBP1 inhibits CcRCC cell proliferation, invasion, and migration

To explore EIF4EBP1's role in ccRCC, RT-qPCR was performed to assess its expression in ccRCC cell lines. As shown in Fig. 10A, EIF4EBP1 levels were markedly increased in 786-O, 769-P, and OS-RC-2 cells relative to HK-2 controls. Immunohistochemistry also revealed significantly elevated EIF4EBP1 protein expression in tumor tissues versus normal samples (Fig. 10B and C). Western blot analysis revealed markedly elevated EIF4EBP1 protein levels in 786-O, 769-P, and OS-RC-2 cells relative to HK-2 controls (Fig. 10D). We selected the 786-O cell line for subsequent experiments due to its high EIF4EBP1 expression. EIF4EBP1 knockdown was induced using plasmid-mediated silencing, with efficiency confirmed by Western blot analysis. CCK-8 assays showed that

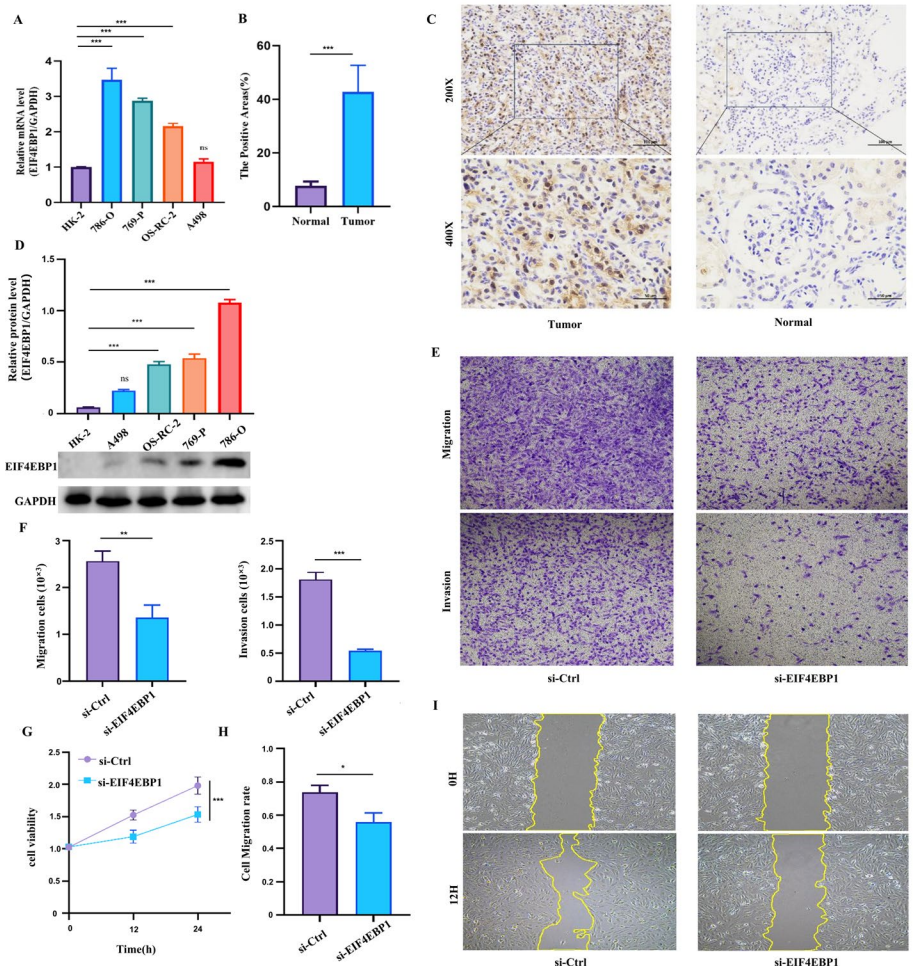


**Fig. 10** EIF4EBP1 Expression and Functional Analysis in ccRCC Cells. **A** RT-qPCR analysis revealed elevated expression levels of EIF4EBP1 in ccRCC cell lines. **B, C** Immunohistochemical staining. **D** EIF4EBP1 protein levels were measured by Western blot. **E, F** The invasion of EIF4EBP1 knockdown was assessed by transwell assay. **G** CCK-8 assay measuring cell viability. **H, I** Wound healing assays measure cell migration potential. (*$p < 0.05$, **$p < 0.01$, ***$p < 0.001$, ns, not significant)

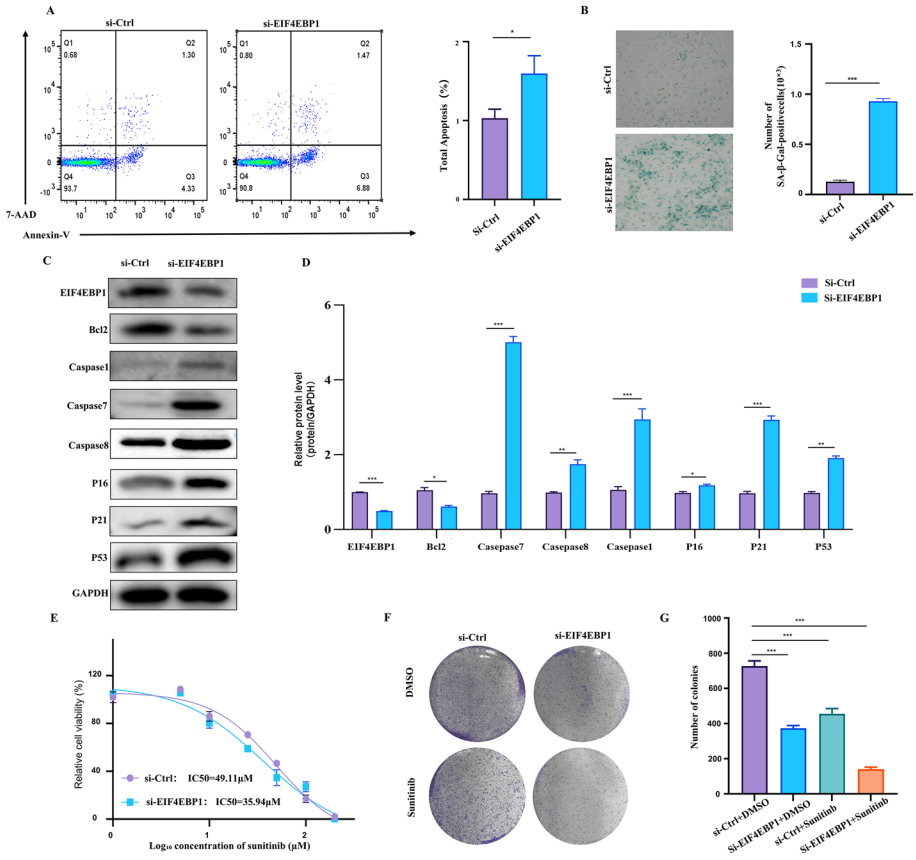


**Fig. 11** EIF4EBP1 knockdown affects cell apoptosis, senescence, and drug sensitivity in ccRCC Cells. **A** Apoptosis in 786-O cells was assessed by flow cytometry using Annexin V and 7-AAD labeling. Representative plots from independent experiments are shown. **B** SA-β-Gal staining was used to evaluate EIF4EBP1 knockdown-induced cellular senescence. **C, D** Western blot analysis measures apoptosis and senescence-related proteins after knockdown of EIF4EBP1. **E** CCK-8 assay evaluating the effect of EIF4EBP1 downregulation on sunitinib-induced cytotoxicity. **F** Colony formation assay of EIF4EBP1-downregulated ccRCC cells, and **G** quantification of colony numbers. (*$p <$ 0.05, **$p <$ 0.01, ***$p <$ 0.001)

EIF4EBP1 silencing markedly decreased cell proliferation (Fig. 10G). Transwell (Fig. 10E, F) and wound healing (Fig. 10H, I) assays indicated that EIF4EBP1 silencing decreased 786-O cell migration and invasion.

### 3.16 Knockdown of EIF4EBP1 enhances CcRCC cell apoptosis and induces senescence-associated phenotypes

Flow cytometry reveals increased apoptosis upon EIF4EBP1 knockdown compared to si-Ctrl group (Fig. 11A). The si-EIF4EBP1 group exhibited enhanced senescence-associated phenotypes, as evidenced by increased SA-β-gal staining intensity (Fig. 11B). We next examined apoptosis- and senescence-related proteins via Western blotting, and the results indicated that EIF4EBP1 knockdown promoted both apoptosis and senescence in ccRCC cells (Fig. 11C and D).

### 3.17 EIF4EBP1 knockdown augments sunitinib's antitumor efficacy

To evaluate the contribution of EIF4EBP1 to tyrosine kinase inhibitor sensitivity, we treated si-Ctrl and si-EIF4EBP1 cells with sunitinib. Gene silencing increased treatment sensitivity, as shown in Fig. 11E. Colony formation assays further revealed that

concurrent EIF4EBP1 knockdown and sunitinib administration dramatically reduced ccRCC cell growth (Fig. 11F and G).

## 4 Discussions

ccRCC is the most prevalent histological subtype of renal carcinoma and a major contributor to cancer-induced mortality [30]. Although therapies such as immunotherapy and tyrosine kinase inhibitors have advanced, metastatic incidence and mortality in ccRCC continue to rise [31]. Cellular senescence represents a state intimately associated with diverse physiological processes and age-related pathologies, typically defined by a permanent halt in the cell cycle [32]. CS is characterized by the induction of the SASP, whereby a diverse array of cytokines, growth factors, chemokines, and proteases are secreted by senescent cells. Through these factors, the TME is remodeled, and processes such as immune evasion, angiogenesis, and resistance to chemotherapy are facilitated [17, 32, 33]. These characteristics emphasize the critical connection between cellular senescence and immune cell infiltration [34]. Therefore, constructing novel prognostic models and identifying potential therapeutic biomarkers are essential for improving clinical outcomes in ccRCC patients.

We successfully constructed the SRGM model for ccRCC patients using various machine learning methods. By combining multiple algorithms, we were able to effectively reduce the dimensionality of the variables, making the model more concise and reliable. Kaplan-Meier survival analysis verified the model's superior predictive capability in survival outcomes. In comparison to 55 existing models, our model exhibited enhanced predictive accuracy, with the risk score emerging as an independent prognostic indicator. The nomogram, constructed by combining risk scores with clinical features, exhibited excellent estimation ability and accuracy, significantly improving the prediction of ccRCC patient prognosis.

Immune cell infiltration is a fundamental characteristic of the TME, exerting a pivotal function in tumor immune evasion and the establishment of an inflammatory milieu [35, 36]. To elucidate the differences in model stratification and provide a basis for treatment strategies, we conducted analysis of immune infiltration, immune checkpoints, and immunotherapy-related factors. Immune infiltration analysis demonstrated that, in contrast to low-risk patients, high-risk patients showed a marked increase in the infiltration of Tregs, M0 macrophages, and CD8 + T cells. Tregs, as a major immunosuppressive cell type, are linked to adverse prognosis in the progression of ccRCC [37]. The pronounced presence of CD8 + T cells in ccRCC correlates with an unfavorable clinical outcome, a relationship that differs from their role in other tumor types [38]. Furthermore, TIDE scores indicated that patients at low risk are more inclined to respond to immunotherapy and derive greater benefit from immune checkpoint blockade (ICB) treatment. In contrast, high-risk ccRCC patients showed increased levels of immune checkpoint gene expression, such as CTLA4, LAG3, and PDCD1, which may reflect an immune-regulatory or dysfunctional tumor microenvironment and have been associated with unfavorable prognosis in specific clinical contexts.LAG-3, an inhibitory receptor, is essential for immune suppression within the TME, highlighting its potential as a therapeutic target for high-risk patients [39]. Furthermore, drug sensitivity analysis identified potentially effective drugs, providing valuable insights for the treatment of ccRCC.

To gain deeper insights, we selected EIF4EBP1, a core gene among the 9 SRGs, for further investigation. EIF4EBP1 (also referred to as 4EBP1) encodes a protein that inhibits translation by competing with the eukaryotic translation initiation factor 4E, consequently reducing protein synthesis [40]. The EIF4EBP1 gene resides in the 8p12 chromosomal region, and amplification of this locus correlates with increased EIF-4EBP1 transcript levels, suggesting that EIF4EBP1 may function as a potential oncogene [41]. EIF4EBP1 has been shown to bind and stabilize the mammalian target of rapamycin complex 1 (mTORC1), thereby facilitating activation of this signaling pathway [42]. Mechanistic studies show that mTORC1-mediated regulation of mitochondrial oxidative phosphorylation results in excessive ROS production. The resulting oxidative damage to critical biomolecules (DNA, proteins, and membrane lipids) constitutes a key molecular mechanism underlying mTORC1-induced cellular senescence [43]. EIF4EBP1 could exert a dual function in tumorigenesis, contributing to both the promotion of tumor progression and the suppression of its initiation [44]. Moreover, research has demonstrated that EIF4EBP1 levels correlate with malignant advancement and poor prognosis in various cancers [45–47]. In a study on colon cancer, downregulation of EIF4EBP1 triggered epithelial-mesenchymal transition, enhanced Snail expression, and facilitated cancer cell migration, invasion, and metastasis [48]. It is reported that EIF4EBP1 can enhance resistance to prostate cancer cells, indicating that EIF4EBP1 may be associated with chemotherapy resistance in human tumors [49]. Furthermore, Karlsson et al. demonstrated that high expression of EIF4EBP1 is related to endocrine therapy resistance in ER/PR-positive patients [50]. We are the first to identify the correlation between EIF-4EBP1 and ccRCC cell proliferation, invasion, senescence, and drug resistance, and we extensively validated these findings through cell experiments.

scRNA-seq revealed pronounced upregulation of EIF4EBP1 in epithelial cells, which were enriched in the high-expression subgroup. Trajectory analysis further showed that EIF4EBP1 expression increased along epithelial pseudotime, consistent with cellular maturation and potentially associated with senescence or functional exhaustion. Given that mitochondrial dysfunction and impaired oxidative phosphorylation are hallmark metabolic features of ccRCC and closely linked to cellular senescence, these findings align with known metabolic vulnerabilities of the disease [51]. Additionally, we analyzed the spatial expression pattern of EIF4EBP1 in ccRCC using spatial transcriptomics. The findings revealed that EIF4EBP1 was upregulated in ccRCC. Silencing EIF4EBP1 expression markedly reduced cellular proliferation, migration, and invasion. Western blot analyses further demonstrated that EIF4EBP1 knockdown promoted apoptosis and cellular senescence in ccRCC cells. Based on these findings and previous reports, EIF4EBP1 may act as a negative regulator of senescence, potentially through activation of the mTORC1 pathway; however, the underlying molecular mechanisms require further investigation [42]. Although sunitinib is a cornerstone therapy for advanced ccRCC, most patients develop resistance within two years [52]. Functional studies revealed that EIF4EBP1 knockdown sensitizes ccRCC cells to sunitinib treatment, suggesting its role in modulating therapeutic efficacy. This reveals EIF4EBP1's therapeutic potential and offers a new targeting approach for sunitinib resistance. Our systematic multi-omics and experimental data establish EIF4EBP1 as a promising ccRCC target, functionally linked to proliferation, invasion, and treatment resistance.

This study has several limitations. First, the reliance on public datasets may not fully capture the clinical heterogeneity of ccRCC, and prospective validation in multicenter cohorts will be necessary to further confirm the predictive value of the prognostic model in real-world settings. Second, although functional experiments demonstrated that EIF-4EBP1 perturbation induces senescence-associated phenotypes and suppresses malignant behaviors, the absence of gain-of-function assays and the lack of direct assessment of EIF4EBP1 phosphorylation status limit mechanistic resolution. Third, drug sensitivity analyses were hypothesis-generating and require further validation in cellular and in vivo models, while immune microenvironment and treatment response analyses, largely based on computational inference and in vitro data, may not fully reflect clinical outcomes. Finally, although single-cell RNA sequencing and spatial transcriptomics provided valuable insights into the cellular localization and transcriptional context of EIF4EBP1, these approaches have inherent limitations in comprehensively capturing tumor heterogeneity. Future studies integrating functional, phospho-proteomic, and longitudinal analyses are warranted to further clarify the role of EIF4EBP1 in ccRCC pathogenesis and therapeutic response.

## 5 Conclusion

This study developed a senescence-based prognostic model for ccRCC, with strong predictive power across datasets. EIF4EBP1, a core gene, promotes tumor progression and drug resistance. Its knockdown inhibited tumor behaviors and improved sunitinib sensitivity, highlighting EIF4EBP1 as a promising therapeutic target and offering insights for personalized ccRCC treatment.

## Supplementary Information

The online version contains supplementary material available at https://doi.org/10.1007/s12672-026-04484-5.

Supplementary Material 1

Supplementary Material 2

Supplementary Material 3

Supplementary Material 4

Supplementary Material 5

Supplementary Material 6

Supplementary Material 7

**Acknowledgements**

We would like to express our gratitude to databases such as TCGA, GEO, and BEST for providing data support, which made our research possible.

**Author contributions**

He Duan: Conceptualization, Data curation, Formal Analysis, Writing – original draft, Writing – review & editing. Ning Li: Investigation, Methodology, Software, Validation, Writing – original draft, Writing – review & editing. Dingming Song: Data curation, Investigation, Software, Writing – review & editing. Yongzhuo Li: Data curation, Software, Writing – review & editing. XinLiang: Data curation, Formal analysis, Writing – original draft. Yongxue Ding: Methodology, Supervision, Writing – review & editing. Ming Tong: Conceptualization, Methodology, Supervision, Writing – original draft, Writing – review & editing. All authors reviewed the manuscript.

**Funding**

The author(s) confirm that no financial support was received for the research, manuscript preparation, or publication of this article.

**Data availability**

The original data presented in this study are included in the article/supplementary material. All datas and code necessary for the analyses are available upon request. For further information, please contact the corresponding author.

## Declarations

### Ethics approval and consent to participate

This study involving human participants was approved by the Ethics Committee of the First Affiliated Hospital of Jinzhou Medical University (Reference No. KYLL202513). All procedures were conducted in accordance with local regulations and institutional guidelines. Written informed consent was obtained from all participants prior to their inclusion in the study.

### Consent for publication

All participants provided written informed consent for the publication of their data.

### Competing interests

The authors declare no competing interests.

Received: 15 September 2025 / Accepted: 20 January 2026

Published online: 11 March 2026

### References

1. Ljungberg B, Albiges L, Abu-Ghanem Y, Bedke J, Capitanio U, Dabestani S, et al. European association of urology guidelines on renal cell carcinoma: the 2022 update. Eur Urol. 2022;82(4):399–410. https://doi.org/10.1016/j.eururo.2022.03.006.
2. Siegel RL, Miller KD, Fuchs HE, Jemal A. Cancer statistics, 2022. CA Cancer J Clin. 2022;72(1):7–33. https://doi.org/10.3322/caac.21708.
3. Lucarelli G, Lasorsa F, Milella M, d'Amati A, Ingravallo G, Silecchia M, et al. Transcriptomic and proteo-metabolic determinants of the grading system in clear cell renal cell carcinoma. Urol Oncol. 2025;43(8):e469419-32. https://doi.org/10.1016/j.urolonc.2025.02.016.
4. Santoni M, Mollica V, Rizzo A, Massari F. Dynamics of resistance to immunotherapy and TKI in patients with advanced renal cell carcinoma. Cancer Treat Rev. 2025. https://doi.org/10.1016/j.ctrv.2025.102881.
5. Rizzo A, Mollica V, Marchetti A, Nuvola G, Rosellini M, Tassinari E, et al. Adjuvant PD-1 and PD-L1 inhibitors and relapse-free survival in cancer patients: the mouseion-04 study. Cancers. 2022. https://doi.org/10.3390/cancers14174142.
6. Al-Danakh A, Safi M, Alradhi M, Chen Q, Baldi S, Zhu X, et al. Immune checkpoint inhibitor (ICI) genes and aging in clear cell renal cell carcinoma (CCRCC): clinical and genomic study. Cells. 2022. https://doi.org/10.3390/cells11223641.
7. Ozay ZI, Jo Y, Fortuna GG, Chehade CH, Gebrael G, Ostrowski M, et al. Treatment and attrition trends for metastatic clear cell renal cell carcinoma in the Us. JAMA Netw Open. 2025. https://doi.org/10.1001/jamanetworkopen.2025.1201.
8. di Meo NA, Lasorsa F, Rutigliano M, Milella M, Ferro M, Battaglia M, et al. The dark side of lipid metabolism in prostate and renal carcinoma: novel insights into molecular diagnostic and biomarker discovery. Expert Rev Mol Diagn. 2023;23(4):297–313. https://doi.org/10.1080/14737159.2023.2195553.
9. Lasorsa F, Rutigliano M, Milella M, Ferro M, Pandolfo SD, Crocetto F, et al. Cancer stem cells in renal cell carcinoma: origins and biomarkers. Int J Mol Sci. 2023. https://doi.org/10.3390/ijms241713179.
10. Jiang M, Zhu D, Zhao D, Liu Y, Li J, Zheng Z. Integrated analysis of clinical outcome of mesenchymal stem cell-related genes in pan-cancer. Curr Genomics. 2024;25(4):298–315. https://doi.org/10.2174/0113892029291247240422060811.
11. Ren Z, Zhang X, Han J. Expression and prognostic significance of ferroptosis-related proteins Slc7a11 and Gpx4 in renal cell carcinoma. Protein Pept Lett. 2023;30(10):868–76. https://doi.org/10.2174/0109298665255704230920063254.
12. Munoz-Espin D, Canamero M, Maraver A, Gomez-Lopez G, Contreras J, Murillo-Cuesta S, et al. Programmed cell senescence during mammalian embryonic development. Cell. 2013;155(5):1104–18. https://doi.org/10.1016/j.cell.2013.10.019.
13. Ovadya Y, Landsberger T, Leins H, Vadai E, Gal H, Biran A, et al. Impaired immune surveillance accelerates accumulation of senescent cells and aging. Nat Commun. 2018. https://doi.org/10.1038/s41467-018-07825-3.
14. Ramu D, Shan TW, Hirpara JL, Pervaiz S. Cellular senescence: silent operator and therapeutic target in cancer. IUBMB Life. 2021;73(3):530–42. https://doi.org/10.1002/iub.2460.
15. Khaghani F, Hemmati M, Ebrahimi M, Salmaninejad A. Emerging multi-omic approaches to the molecular diagnosis of mitochondrial disease and available strategies for treatment and prevention. Curr Genomics. 2024;25(5):358–79. https://doi.org/10.2174/0113892029308327240612110334.
16. Demirci D, Dayanc B, Mazi FA, Senturk S. The jekyll and hyde of cellular senescence in cancer. Cells. 2021. https://doi.org/10.3390/cells10020208.
17. Faget DV, Ren Q, Stewart SA. Unmasking senescence: context-dependent effects of Sasp in cancer. Nat Rev Cancer. 2019;19(8):439–53. https://doi.org/10.1038/s41568-019-0156-2.
18. Tufail M, Huang Y-Q, Hu J-J, Liang J, He C-Y, Wan W-D, et al. Cellular aging and senescence in cancer: a holistic review of cellular fate determinants. Aging Dis. 2025. https://doi.org/10.14336/ad.2024.0421.
19. Moskalev AA, Aliper AM, Smit-McBride Z, Buzdin A, Zhavoronkov A. Genetics and epigenetics of aging and longevity. Cell Cycle. 2014;13(7):1063–77. https://doi.org/10.4161/cc.28433.
20. Safwan-Zaiter H, Wagner N, Wagner K-D. P16ink4a-more than a senescence marker. Life. 2022. https://doi.org/10.3390/life12091332.
21. Milella M, Rutigliano M, Pandolfo SD, Aveta A, Crocetto F, Ferro M, et al. The metabolic landscape of cancer stem cells: insights and implications for therapy. Cells. 2025. https://doi.org/10.3390/cells14100717.
22. Liu H, Zhang W, Zhang Y, Adegboro AA, Fasoranti DO, Dai L, et al. Mime: a flexible machine-learning framework to construct and visualize models for clinical characteristics prediction and feature selection. Comput Struct Biotechnol J. 2024;23:2798–810. https://doi.org/10.1016/j.csbj.2024.06.035.
23. Thorsson V, Gibbs DL, Brown SD, Wolf D, Bortone DS, Ou Yang TH, et al. The immune landscape of cancer. Immunity. 2018;48(4):812-e830814. https://doi.org/10.1016/j.immuni.2018.03.023.
24. Zhang F, Li X, Tian W. Unsupervised inference of developmental directions for single cells using vector. Cell Rep. 2020. https://doi.org/10.1016/j.celrep.2020.108069.
25. Wu Y, Yang S, Ma J, Chen Z, Song G, Rao D, et al. Spatiotemporal immune landscape of colorectal cancer liver metastasis at single-cell level. Cancer Discov. 2022;12(1):134–53. https://doi.org/10.1158/2159-8290.Cd-21-0316.

26. Wang H, Liu H, Tang X, Chen J, Ren Z. Editorial: the role of tumor microenvironment in the development, treatment and prognosis of hepatocellular carcinoma. Front Pharmacol. 2024. https://doi.org/10.3389/fphar.2023.1343175.
27. de Visser KE, Joyce JA. The evolving tumor microenvironment from cancer initiation to metastatic outgrowth. Cancer Cell. 2023;41(3):374–403. https://doi.org/10.1016/j.ccell.2023.02.016.
28. Low V, Li Z, Blenis J. Metabolite activation of tumorigenic signaling pathways in the tumor microenvironment. Sci Signal. 2022. https://doi.org/10.1126/scisignal.abj4220.
29. Curry WT, Lim M. Immunomodulation: checkpoint blockade etc. Neuro-Oncology. 2015;17:26–31. https://doi.org/10.1093/neuonc/nov174.
30. Hsieh JJ, Purdue MP, Signoretti S, Swanton C, Albiges L, Schmidinger M, et al. Renal cell carcinoma. Nat Rev Dis Primers. 2017. https://doi.org/10.1038/nrdp.2017.9.
31. Raghubar AM, Matigian NA, Crawford J, Francis L, Ellis R, Healy HG, et al. High risk clear cell renal cell carcinoma microenvironments contain protumour immunophenotypes lacking specific immune checkpoints. NPJ Precis Oncol. 2023. https://doi.org/10.1038/s41698-023-00441-5.
32. Gorgoulis V, Adams PD, Alimonti A, Bennett DC, Bischof O, Bishop C, et al. Cellular senescence: defining a path forward. Cell. 2019;179(4):813–27. https://doi.org/10.1016/j.cell.2019.10.005.
33. Basisty N, Kale A, Jeon OH, Kuehnemann C, Payne T, Rao C, et al. A proteomic atlas of senescence-associated secretomes for aging biomarker development. PLoS Biol. 2020. https://doi.org/10.1371/journal.pbio.3000599.
34. Schneider JL, Rowe JH, Garcia-de-Alba C, Kim CF, Sharpe AH, Haigis MC. The aging lung: physiology, disease, and immunity. Cell. 2021;184(8):1990–2019. https://doi.org/10.1016/j.cell.2021.03.005.
35. Tower H, Ruppert M, Britt K. The immune microenvironment of breast cancer progression. Cancers (Basel). 2019. https://doi.org/10.3390/cancers11091375.
36. Zhang J, Jia Z, Zhang J, Mu X, Ai L. Identification of M2 macrophage-related genes associated with diffuse large B-cell lymphoma via bioinformatics and machine learning approaches. Biol Direct. 2025. https://doi.org/10.1186/s13062-025-00649-4.
37. Cable DM, Murray E, Zou LS, Goeva A, Macosko EZ, Chen F, et al. Robust decomposition of cell type mixtures in spatial transcriptomics. Nat Biotechnol. 2022;40(4):517–26. https://doi.org/10.1038/s41587-021-00830-w.
38. Murakami T, Tanaka N, Takamatsu K, Hakozaki K, Fukumoto K, Masuda T, et al. Multiplexed single-cell pathology reveals the association of Cd8 T-cell heterogeneity with prognostic outcomes in renal cell carcinoma. Cancer Immunol Immunother. 2021;70(10):3001–13. https://doi.org/10.1007/s00262-021-03006-2.
39. Mullard A. Lag3 pushes immuno-oncology's leading edge. Nat Rev Drug Discov. 2022;21(3):167–70. https://doi.org/10.1038/d41573-022-00036-y.
40. Qin X, Jiang B, Zhang Y. 4e-Bp1, a multifactor regulated multifunctional protein. Cell Cycle. 2016;15(6):781–6. https://doi.org/10.1080/15384101.2016.1151581.
41. Karlsson E, Waltersson MA, Bostner J, Perez-Tenorio G, Olsson B, Hallbeck A-L, et al. High-Resolution genomic analysis of the 11q13 amplicon in breast cancers identifies synergy with 8p12 Amplification, involving the Mtor targets S6k2 and 4ebp1. Genes Chromosomes Cancer. 2011;50(10):775–87. https://doi.org/10.1002/gcc.20900.
42. Zarzycka W, Kobak KA, King CJ, Peelor FF, Miller BF, Chiao YA. Hyperactive Mtorc1/4ebp1 signaling dysregulates proteostasis and accelerates cardiac aging. Geroscience. 2025;47(2):1823–36. https://doi.org/10.1007/s11357-024-01368-w.
43. Zoncu R, Efeyan A, Sabatini DM. Mtor: from growth signal integration to cancer, diabetes and ageing. Nat Rev Mol Cell Biol. 2011;12(1):21–35. https://doi.org/10.1038/nrm3025.
44. Martineau Y, Azar R, Bousquet C, Pyronnet S. Anti-oncogenic potential of the Eif4e-binding proteins. Oncogene. 2013;32(6):671–7. https://doi.org/10.1038/onc.2012.116.
45. Cha Y-L, Li P-D, Yuan L-J, Zhang M-Y, Zhang Y-J, Rao H-L, et al. Eif4ebp1 overexpression is associated with poor survival and disease progression in patients with hepatocellular carcinoma. PLoS One. 2015. https://doi.org/10.1371/journal.pone.0117493.
46. Kim YY, Von Weymarn L, Larsson O, Fan D, Underwood JM, Peterson MS, et al. Eukaryotic initiation factor 4e binding protein family of proteins: sentinels at a translational control checkpoint in lung tumor defense. Cancer Res. 2009;69(21):8455–62. https://doi.org/10.1158/0008-5472.Can-09-1923.
47. Ouyang Y, Ou Z, Zhong W. Re: Fgfr3 alterations in bladder cancer stimulate serine synthesis to induce immune-inert macrophages that suppress T-cell recruitment and activation. J Urol. 2024;212(3):523–523. https://doi.org/10.1158/0008-5472.
48. Cai W, Ye Q, She Q-B. Loss of 4e-Bp1 function induces Emt and promotes cancer cell migration and invasion via cap-dependent translational activation of snail. Oncotarget. 2014;5(15):6015–27. https://doi.org/10.18632/oncotarget.2109.
49. Hsieh AC, Hao GN, Wen L, Edlind MP, Carroll PR, Kim W, et al. Cell type-specific abundance of 4ebp1 Primes prostate cancer sensitivity or resistance to Pi3k pathway inhibitors. Sci Signal. 2015. https://doi.org/10.1126/scisignal.aad5111.
50. Karlsson E, Perez-Tenorio G, Amin R, Bostner J, Skoog L, Fornander T, et al. The Mtor effectors 4ebp1 and S6k2 are frequently coexpressed, and associated with a poor prognosis and endocrine resistance in breast cancer: a retrospective study including patients from the randomised Stockholm tamoxifen trials. Breast Cancer Res. 2013. https://doi.org/10.1186/bcr3557.
51. De Marco S, Torsello B, Minutiello E, Morabito I, Grasselli C, Bombelli S, et al. The cross-talk between Abl2 tyrosine kinase and Tgfβ1 signalling modulates the invasion of clear cell renal cell carcinoma cells. FEBS Lett. 2023;597(8):1098–113. https://doi.org/10.1002/1873-3468.14531.
52. Li Q, Zhang Z, Fan Y, Zhang Q. Epigenetic alterations in renal cell cancer with Tkis resistance: from mechanisms to clinical applications. Front Genet. 2021. https://doi.org/10.3389/fgene.2020.562868.


## Publisher's note